



UNIVERSITY OF LEEDS

This is a repository copy of *Heat transfer processes in parallel-plate heat exchangers of thermoacoustic devices - Numerical and experimental approaches*.

White Rose Research Online URL for this paper:  
<http://eprints.whiterose.ac.uk/79881/>

Version: Accepted Version

---

**Article:**

Jaworski, AJ and Piccolo, A (2012) Heat transfer processes in parallel-plate heat exchangers of thermoacoustic devices - Numerical and experimental approaches. *Applied Thermal Engineering*, 42. 145 - 153. ISSN 1359-4311

<https://doi.org/10.1016/j.applthermaleng.2012.03.014>

---

**Reuse**

Unless indicated otherwise, fulltext items are protected by copyright with all rights reserved. The copyright exception in section 29 of the Copyright, Designs and Patents Act 1988 allows the making of a single copy solely for the purpose of non-commercial research or private study within the limits of fair dealing. The publisher or other rights-holder may allow further reproduction and re-use of this version - refer to the White Rose Research Online record for this item. Where records identify the publisher as the copyright holder, users can verify any specific terms of use on the publisher's website.

**Takedown**

If you consider content in White Rose Research Online to be in breach of UK law, please notify us by emailing [eprints@whiterose.ac.uk](mailto:eprints@whiterose.ac.uk) including the URL of the record and the reason for the withdrawal request.



[eprints@whiterose.ac.uk](mailto:eprints@whiterose.ac.uk)  
<https://eprints.whiterose.ac.uk/>

# Heat transfer processes in parallel-plate heat exchangers of thermoacoustic devices – numerical and experimental approaches

Artur J Jaworski <sup>1,\*</sup> and Antonio Piccolo <sup>2</sup>

<sup>1</sup> Department of Engineering, University of Leicester LE1 7RH, United Kingdom

<sup>2</sup> Department of Civil Engineering, University of Messina, Contrada di Dio – 98166 S. Agata (Messina), Italy

## Abstract

This paper addresses the issues of heat transfer in oscillatory flow conditions, which are typically found in thermoacoustic devices. The analysis presented concerns processes taking place in the individual “channels” of the parallel-plate heat exchangers (HX), and is a mixture of experimental and numerical approaches. In the experimental part, the paper describes the design of experimental apparatus to study the thermal-fluid processes controlling heat transfer in thermoacoustic heat exchangers on the micro-scale of the individual channels. Planar Laser Induced Fluorescence (PLIF) and Particle Image Velocimetry (PIV) techniques are applied to obtain spatially and temporally resolved temperature and velocity fields within the HX channels. The temperature fields allow obtaining the local and global, phase-dependent heat transfer rates and Nusselt numbers, and their dependence on the Reynolds number of the oscillating flow. The numerical part of the paper deals with the implementation of CFD modelling capabilities to capture the physics of thermal-fluid processes in the micro-scale and to validate the models against the experimental data. A two-dimensional low Mach number computational model is implemented to analyze the time-averaged temperature field and heat transfer rates in a representative domain of the HXs. These are derived by integrating the thermoacoustic equations of the standard linear theory into a numerical calculus scheme based on the energy balance. The comparisons between the experimental and numerical results in terms of temperature and heat transfer distributions suggest that the optimal performance of heat exchangers can be achieved when the gas displacement amplitude is close to the length of hot and cold heat exchanger. Heat transfer coefficients from the gas-side can be predicted with a confidence of about 40% at moderate acoustic Reynolds numbers.

**Keywords:** Heat Transfer; Heat Exchangers; Thermoacoustic Engines and Coolers; Oscillatory Flow, Experimental, Numerical

---

\* Corresponding author: Tel: +44(0)116 223 1033; Fax: +44(0)116 252 2525; E-mail: a.jaworski@le.ac.uk

## Nomenclature

$a$	speed of sound ( $\text{m s}^{-1}$ )
$A$	surface area ( $\text{m}^2$ )
$c_p$	isobaric specific heat ( $\text{J kg}^{-1}\text{K}^{-1}$ )
$d$	dimension of the square side of the cross section of the resonator
$\dot{e}$	energy flux density ( $\text{Wm}^{-2}$ )
$\bar{e}$	time averaged energy flux density ( $\text{Wm}^{-2}$ )
$f$	spatially averaged $h$ function, resonance frequency (Hz)
$h$	thermoviscous function, specific enthalpy ( $\text{J m}^{-3}$ ), heat transfer coefficient ( $\text{Wm}^2\text{K}^{-1}$ )
$j$	imaginary unit
$k$	wave number ( $\text{m}^{-1}$ ), thermoviscous function (m)
$K$	gas thermal conductivity ( $\text{Wm}^{-1}\text{K}^{-1}$ )
$l$	half fin thickness (m)
$L$	heat exchanger length (m)
Nu	Nusselt number
$p_1$	acoustic pressure amplitude (Pa)
$p_C$	pressure amplitude at the joint and centre of the channel (Pa)
$P_A$	pressure amplitude at a pressure antinode (Pa)
Pr	Prandtl number
$\bar{q}$	time-averaged heat flux density ( $\text{W m}^{-2}$ )
Re	Reynolds number
$t$	time (s)
$T$	instantaneous fluid temperature (K)
$T_1$	amplitude of oscillating temperature (K)
$T_w$	wall (fin) temperature (K)
$T_H$	temperature of the hot fin (K)
$T_C$	temperature of the cold fin (K)
T01-T12	thermocouples
$u$	specific internal energy ( $\text{J m}^{-3}$ )
$v_{x1}$	amplitude of longitudinal velocity ( $\text{m s}^{-1}$ )
$v_{y1}$	amplitude of transverse velocity ( $\text{m s}^{-1}$ )
$v_C$	velocity amplitude at the joint and centre of the channel ( $\text{m s}^{-1}$ )
$x$	axial coordinate/direction (m)
$x_s$	HXs coordinate (m)
$y$	transverse coordinate/direction (m)
$y_0$	half fin spacing (m)

## Greek symbols

$\beta$	thermal expansion coefficient ( $\text{K}^{-1}$ )
$\gamma$	ratio of isobaric to isochoric specific heat
$\delta$	penetration depth, m
$\Delta z$	HX length along the $z$ direction
$\eta$	shear viscosity coefficient ( $\text{N m}^{-2} \text{s}^{-1}$ )
$\theta$	dimensionless temperature, $(T-T_w)/(T_H-T_C)$
$\kappa$	gas thermal diffusivity ( $\text{m}^2 \text{s}^{-1}$ )
$\lambda$	wavelength of the sound wave (m)
$\nu$	kinematic viscosity ( $\text{m}^2\text{s}^{-1}$ )
$\xi$	generic acoustic variable
$\xi_C$	displacement amplitude at the joint and centre of the channel (m)
$\rho$	density of the gas ( $\text{kg m}^{-3}$ )
$\sigma$	component of the viscosity stress tensor ( $\text{N m}^{-2} \text{s}^{-2}$ )
$\tau$	component of the viscosity stress tensor ( $\text{N m}^{-2} \text{s}^{-2}$ )
$\Phi$	phase of the acoustic cycle (deg, rad)
$\omega$	angular frequency ( $\text{rad s}^{-1}$ )
$\Omega$	blockage ratio

## Subscripts

0	mean, time averaged
1	first order acoustic variable
$A$	acoustic amplitude at a pressure antinode
$HX$	referring to the HX
$P$	isobaric
$Res$	resonator
$X$	longitudinal, $x$ -component
$Y$	transverse, $y$ -component
$Z$	along the $z$ direction
$\kappa$	thermal
$\nu$	viscous

## 1. Introduction

Thermoacoustic technologies are concerned with developing new concepts of engines, coolers and heat pumps which operate on the basis of a range of thermoacoustic effects. These are broadly understood as energy transfer between a compressible fluid and solid boundary in the presence of an acoustic wave. The correct phasing between the acoustically-induced fluid displacement and its compression or expansion, coupled with heat transfer processes between the solid and fluid, will lead to the implementation of Stirling-like thermodynamic cycles which are of practical engineering importance. A number of practical thermoacoustic devices, both standing- and travelling-wave, have already been demonstrated [1, 2].

There are significant advantages of utilising thermoacoustic technologies, in certain areas of application. Firstly, as there are no moving components, the thermoacoustic devices can be around one order of magnitude cheaper than many conventional cycles (e.g. typical Stirling machine) and can offer longevity and low maintenance costs. In addition, as the thermodynamic cycle uses environmentally benign noble/inert gases as the working medium, there are significant environmental benefits of the technology. Finally, thermoacoustic systems scale very well and are ideal for utilising the low grade heat input (waste heat from industrial processes and solar energy and other forms of energy harvesting) which offers new opportunities for energy conservation.

A typical thermoacoustic device consists of (i) an acoustic network, (ii) an electro-acoustic transducer, (iii) a porous solid medium (namely a regenerator in travelling-wave systems [3] or a stack in standing-wave systems [4]) and (iv) at least a pair of heat exchangers (HXs) [5]. The stack/regenerator is the component where the desired heat/sound energy conversion takes place. “Hot” and “cold” heat exchangers (CHX and HHX, respectively), placed in close proximity of both ends of the stack/regenerator, absorb (or supply) energy from (or to) its ends thus enabling heat communication with external heat sources and sinks.

It is worth noting at this point that compared to the well-known types of HXs for steady flows HXs in the thermoacoustic context provide a range of new challenges. This is due to the fact that the flow is oscillatory. While the existing knowledge for steady flow arrangements is of little practical value [6,7], the relevant investigations in the oscillatory flow are very scarce [8-10]. Therefore, this work is driven by the need for a better understanding and quantitative description of heat transfer under oscillatory flow conditions in thermoacoustic HXs with the aim of improving the overall system performance. The research presented in this paper had two types of activities carried out in tandem. Firstly, experimental facilities had to be developed for careful investigations of the thermal-fluid processes within the individual channels of parallel plate HXs. Secondly, CFD modelling capabilities had to be developed in order to capture the physics of thermal-fluid processes and to validate the models against the experimental data. In order to simplify as much as possible the experimental implementation and the numerical modelling the physical arrangement of the HXs was simplified compared to real thermoacoustic devices. In particular, only a pair of “mock-up” HXs is studied, with no stack/regenerator installed between them. These parallel-plate type HXs are arranged side by side with no gap between them.

The experimental activities involved two-dimensional temperature and velocity field measurements using Planar Laser Induced Fluorescence (PLIF) and Particle Image Velocimetry (PIV) techniques, respectively, to obtain spatially and temporally resolved temperature and velocity fields within the thermoacoustic HX samples. On the basis of recorded temperature fields, the experimental data were processed to obtain the local and global, phase-dependent heat transfer

rates and Nusselt numbers, and their dependence on the Reynolds number of the oscillating flow. The CFD modelling entailed the development of a two-dimensional low Mach number computational model to analyze the time-averaged temperature field and heat transfer rates in a representative domain of the HXs. These were generated by integrating the thermoacoustic equations of the standard linear theory into an energy balance-based numerical calculus scheme. The model accounts for hydrodynamic heat transport along the transverse direction normal to the fin surfaces, temperature dependent thermophysical gas/solid parameters and flow losses. The comparison between simulation results and experiments is based on the phase-averaged temperature fields and on the integrated data of heat flux and Nusselt number. This work is the first attempt of its kind to validate the heat transfer prediction codes in the context of a thermoacoustic device by the detailed in-situ measurements of temperature fields obtained for an individual pore/channel of the heat exchanger assembly. Therefore, it is hoped that the results of this work constitute an important scientific and technological foundation for future improvements of the performance of thermoacoustic engines where this is dependent on heat communication.

## 2. Experimental setup

The general schematic of the experimental apparatus and the PLIF instrumentation is shown in Fig. 1. The experimental apparatus consists of a 7.4 m long resonator of a square internal cross section. It is joined with a cubical loudspeaker box with a side length of 0.6 m through a 0.3 m long transition part, which increases the cross section from 134 mm × 134 mm on its resonator end to 500 mm × 500 mm on the box end. The resonator is filled with nitrogen at atmospheric pressure and room temperature. A subwoofer type loudspeaker is used to generate a standing wave of one quarter wavelength mode in the resonator, at a frequency ( $f$ ) of 13.1 Hz.

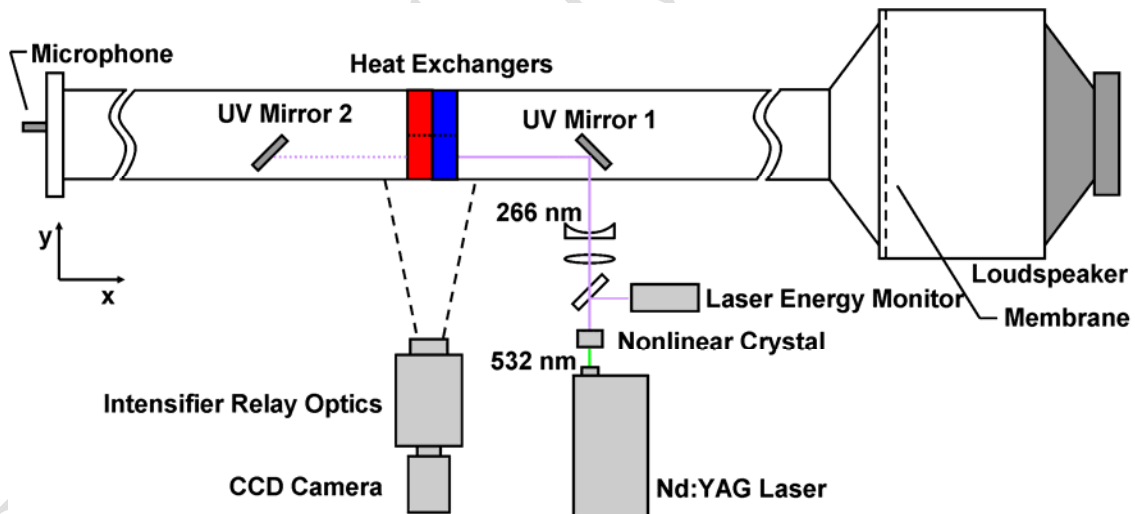


**Figure 1.** Schematic drawing of the experimental apparatus with a PLIF system

A sinusoidal signal from a function generator (TTi TG1010A) is sent to a power amplifier, whose output is then connected to the loudspeaker. The acoustic oscillation amplitude is varied by controlling the amplitude of the sinusoidal signal from the function generator. The acoustic pressure is monitored by a microphone (B&K Model 4136) flush-mounted on the end plate of the resonator. The pressure signal from the microphone is also used as a phase reference for Planar Laser Induced Fluorescence (PLIF) imaging.

A pair of “mock-up” HXs was placed in the resonator, about 4.6 m (0.17 of the wavelength) from the closed end of the resonator. The configuration of the HX pair is schematically shown in Fig. 2a, with a photograph of the actual implementation shown in Fig. 2b. Each HX consists of five active fins and eight dummy aluminium fins to fill up the whole cross-section of the resonator. Each hot HX fin is made out of a brass plate with a cable heater embedded in a prepared channel (Fig. 2c). High-temperature epoxy was applied to fill up the channel and form a flat surface. Each cold HX fin is also made out of a brass plate, with a wide meandering channel prepared for water circulation (Fig. 2c). Water inlet and outlet are connected to the channel ends via steel tubing. The channel was covered with a thin brass sheet, which was soldered on top; the whole assembly was further machined to obtain a flat surface. All fins are 3.2 mm thick ( $2l$ ) and 35 mm long ( $L$ ) in the direction of the oscillating flow, with a span-wise width ( $\Delta z$ ) of 132 mm.

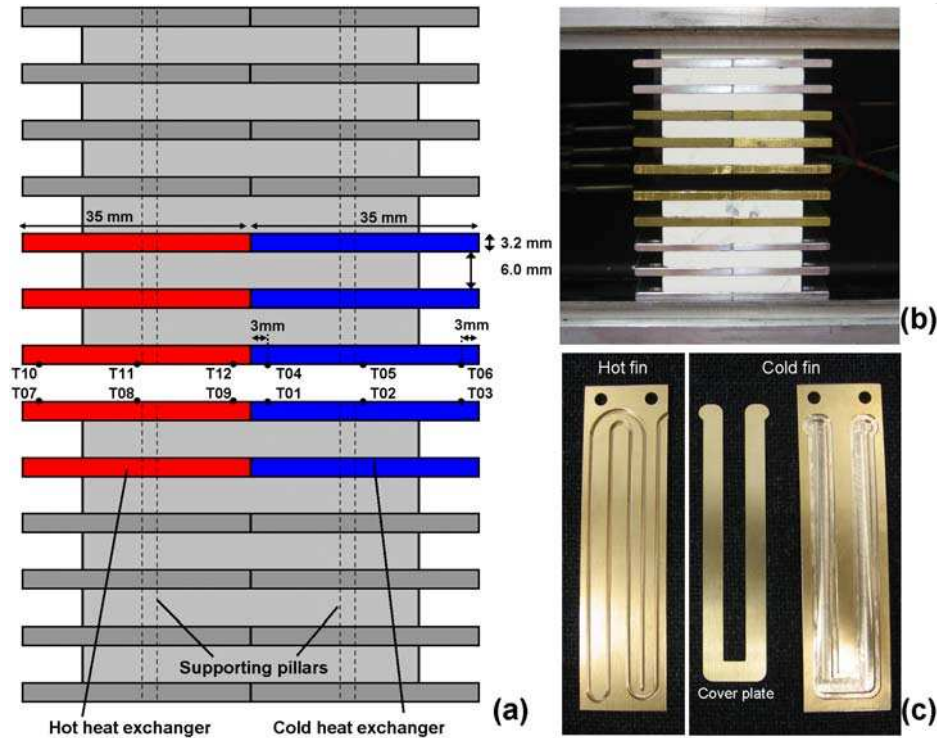


**Figure 2.** Schematic of the configuration of the heat exchangers (a); photograph of the physical implementation (b); photograph of machined hot (left) and cold (right) heat exchanger fins (c)

Ceramic spacers ( $6 \text{ mm} \times 10 \text{ mm} \times 50 \text{ mm}$ ) were used in the front, as well as in the back (not shown) to maintain the channel height ( $2y_0$ ) at 6.0 mm, and also to prevent the channel from severe deformation due to the thermal stresses in the fins. These ceramic blocks and HX fins were strengthened by supporting pillars. Only one channel, in the centre of the resonator, was left unobstructed for PLIF imaging.

The surface temperature of the HX fins that form the channel under investigation were monitored by using twelve K-type thermocouples (Fig. 2a). They are mounted in the centre of the fins in the span-wise direction. Four thermocouples (i.e. “T01”, “T04”, “T09” and “T12”) are 3 mm away from the joint between hot and cold fins. Another four are in the middle of the cold (“T02” and “T05”) and hot (“T08” and “T11”) fins. The last four (“T03”, “T06”, “T07” and “T10”) are placed 3 mm away from the far edge of the cold and hot fins. The heating on the hot fins was controlled by a PID-mode temperature controller, which maintained a preset temperature value (e.g.  $200 \text{ }^\circ\text{C}$ ) at the monitored point (“T07”) within the range of  $\pm 1 \text{ }^\circ\text{C}$ . Due to the thermal contact on the joints between hot and cold fins in the present arrangement, unwanted heat conduction was introduced, which makes the surface temperatures on the hot and cold fins decrease from

left to right. The maximum temperature difference between “T07” and “T09” or between “T10” and “T12” can be up to 20°C. It is known from tests that the surface temperature on the fins along the span-wise direction was nearly constant.

Before the temperature field measurement, the flow velocity fields were obtained with Particle Image Velocimetry (PIV) techniques. The velocity amplitude ( $v_c$ ), at the joint and centre of the channel, and the corresponding displacement amplitude of gas parcel ( $\xi_c = v_c/\omega$ , where  $\omega$  is the angular frequency) were varied from 1.3 m/s to 3.84 m/s and from 16 mm to 46 mm respectively. The corresponding acoustic Reynolds numbers based on the thickness ( $2l$ ) of the fin ( $Re = v_c 2l/\nu$ ) –  $\nu$  being the kinematic viscosity – varied from 250 to 702.

Temperature field measurements were then carried out at the same oscillation amplitude, by employing a PLIF system (LaVision) as shown in Fig. 1. Acetone was used as the fluorescent tracer. UV light sheet at 266 nm is generated by a Nd:YAG laser. It enters the resonator perpendicularly to its axis through a quartz window of 3 mm thickness, is reflected by a UV mirror and becomes parallel to the resonator axis and normal to the surface of the heat exchanger plates. The laser sheet plane was 33 mm away from the front end of the heat exchangers, rather than at the centre of the HXs (Fig. 1), to avoid the effect of the surface mounted thermocouples on the flow and temperature fields. Two UV mirrors were used, to enable the investigation of the temperature fields inside and outside of the channel. The laser could be moved along the resonator side wall by using an automated traverse system to use either of the two UV mirrors as necessary. The UV mirrors are placed 300 mm away from the heat exchanger not to disturb the flow and temperature fields around the heat exchangers. Quartz windows are mounted on the resonator at the locations of the heat exchangers and the mirrors for their higher transmission to UV and fluorescence emissions.

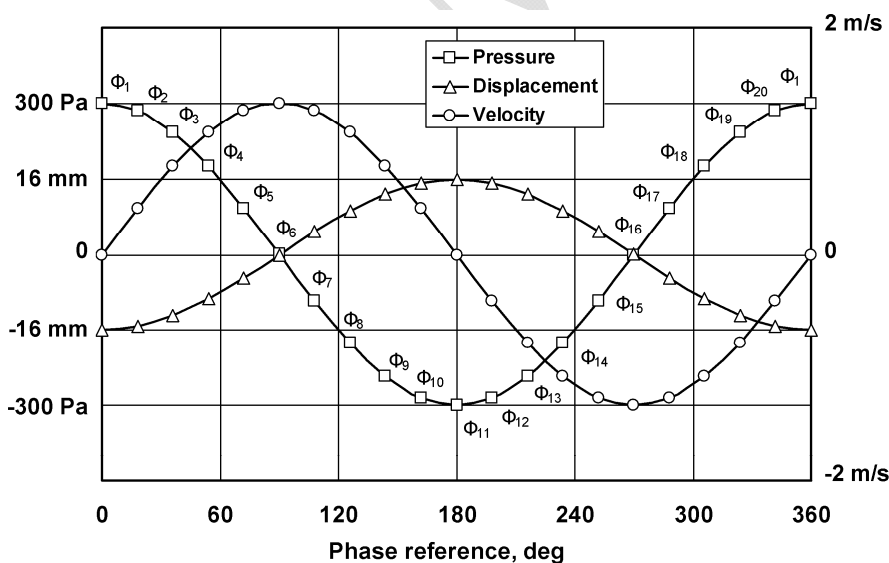


**Figure 3.** Reference pressure, displacement and velocity variation in an acoustic cycle and the investigated 20 phases. The gas displacement amplitude is 16mm.

Acetone of optimal concentration was seeded into the flow by a purpose-designed seeding mechanism. PLIF images were captured by an intensified CCD camera. Images with effective pixels of  $1024 \times 1024$  were obtained, giving a spatial resolution of  $64\mu\text{m}$  per pixel. Images were post-processed using LaVision DaVis 7.2 software package. Three views were recorded with one next to another in the longitudinal direction to cover the area stretching beyond the length of the channel in front of the hot/cold HX fins. Prior to the acquisition of experimental measurement of temperature fields, additional calibration procedure was undertaken to establish the correlation between the fluorescence intensity

and the fluid temperature. Further information about the temperature measurement with PLIF techniques can be found in [11].

Measurements of temperature and velocity fields were carried out for 20 phases within an acoustic cycle as illustrated in Fig. 3, which shows the measured reference pressure  $p_C$ , the measured velocity  $v_C$  and the calculated displacement  $\xi_C$ . The directions of the velocity and displacement are defined within the coordinate system given in Fig. 1. For each phase, 100 frames were taken to calculate the phase-averaged temperature field. The increase of the number of frames beyond 100 provides negligible accuracy gains in terms of the resulting temperature fields.

### 3. Computational model

The numerical model used in this study is the same as that applied in [12], so a more synthetic description is given here. For additional information the reader is directed to [12]. The periodicity of the HXs structure along the transverse  $y$  direction allows calculations to be performed in a single channel of the HX assembly. The computational domain is further reduced by symmetry from half a gas duct to the solid surfaces of the coupled hot and cold fins which are treated as two isothermal surfaces respectively at temperature  $T_H$  and  $T_C$  (see Fig. 4).

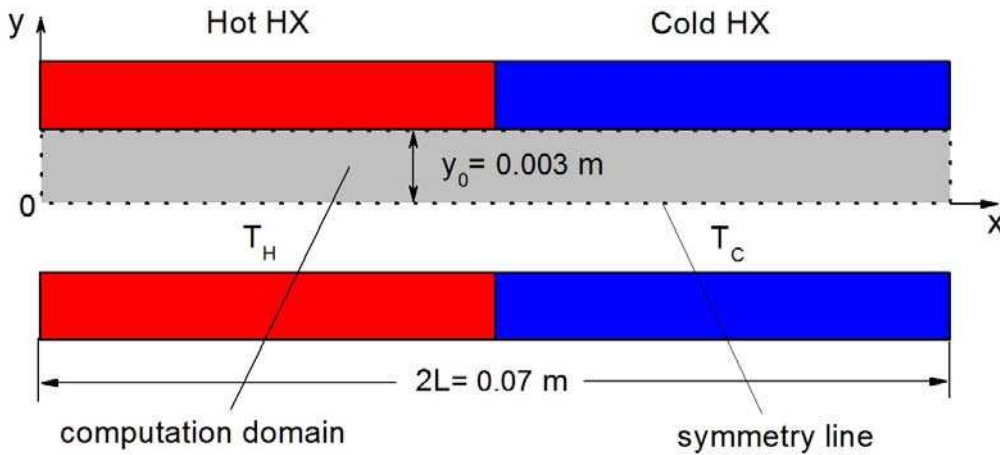


**Figure 4.** Magnified view of the computational domain (light grey area)

The implementation of the numerical model relies on a number of assumptions: The problem is considered as two-dimensional. The processes taking place are within a low Mach number regime, so that any acoustic variable  $\xi$  can be expressed in the complex notation by the conventional first-order expansion  $\xi(x, y, t) = \xi_0(x, y) + \text{Re} \{ \xi_1(x, y) e^{j\omega t} \}$ , where  $t$  is the time,  $j$  the imaginary unit,  $\omega$  the angular frequency,  $\xi_0$  the (real) mean value,  $\xi_1$  the (complex) amplitude of oscillation, and where  $\text{Re} \{ \}$  denotes the real part. The fluid is Newtonian and obeys the ideal gas state equation. Temperature dependent thermo-physical gas parameters are used in the model. HXs are significantly shorter than the acoustic wavelength and acoustically non-intrusive so that the acoustic field can be approximated in the HX neighbourhood by a 1D lossless standing wave:

$$p_1 = P_A \cos(kx_s) = p_0 \quad v_{x1} = j \frac{P_A}{\rho_0 a} \sin(kx_s) = jv_0 \quad (1)$$

where  $p_1$  is the amplitude of the dynamic pressure,  $P_A$  is the amplitude of the dynamic pressure at a pressure anti-node,  $v_{x1}$  is the amplitude of the longitudinal particle velocity,  $k$  is the wave number ( $k=2\pi/\lambda$ ),  $a$  is the sound velocity and  $x_s$  the distance of the HXs from the closed end of the resonator.

Amplitudes of the oscillating temperature  $T_1$ , longitudinal velocity  $v_{x1}$ , transverse gradient of the longitudinal velocity  $\partial v_{x1}/\partial y$ , transverse velocity  $v_{y1}$  and transverse gradient of the transverse velocity  $\partial v_{y1}/\partial y$  inside a gas pore are described by the standard equations of the classical thermoacoustic theory. According to the assumption that the specific heats of the plate/fin materials are notably greater than the isobaric specific heat of the gas  $c_p$  (i.e. temperature oscillations in the solid are negligible), the following equations can be formulated [1,6]:

$$T_1 = \frac{1}{\rho_0 c_p} (1 - h_\kappa) p_1 - \frac{1}{\rho_0 \omega^2 (1 - \text{Pr})} \frac{dp_1}{dx} \frac{\partial T_0}{\partial x} [(1 - h_\kappa) - \text{Pr}(1 - h_\nu)] \quad (2)$$

$$v_{x1} = \frac{j}{\omega \rho_0} \frac{dp_1}{dx} (1 - h_\nu) \quad (3)$$

$$\frac{\partial v_{x1}}{\partial y} = \frac{2}{\omega \rho_0 \delta_\nu^2} \frac{dp_1}{dx} k_\nu \quad (4)$$

$$v_{y1} = j \frac{\omega}{\rho_0 a^2} \left\{ \frac{[1 + (\gamma - 1)f_\kappa](y - k_\nu) - [y + (\gamma - 1)k_\kappa](1 - f_\nu)}{(1 - f_\nu)} \right\} p_1 + j \frac{\beta}{\rho_0 \omega (1 - \text{Pr})} \left\{ \frac{f_\nu(y - k_\kappa) - f_\kappa(y - k_\nu) + (k_\kappa - k_\nu)}{(1 - f_\nu)} \right\} \frac{\partial T_0}{\partial x} \frac{dp_1}{dx} \quad (5)$$

$$\frac{\partial v_{y1}}{\partial y} = j \frac{\omega}{\rho_0 a^2} \left\{ \frac{[1 + (\gamma - 1)f_\kappa](1 - h_\nu) - [1 + (\gamma - 1)h_\kappa](1 - f_\nu)}{(1 - f_\nu)} \right\} p_1 + j \frac{\beta}{\rho_0 \omega (1 - \text{Pr})} \left[ \frac{f_\nu(1 - h_\kappa) - f_\kappa(1 - h_\nu) + (h_\kappa - h_\nu)}{(1 - f_\nu)} \right] \frac{\partial T_0}{\partial x} \frac{dp_1}{dx} \quad (6)$$

where

$$h_\kappa = \frac{\cosh[(1 + j)y/\delta_\kappa]}{\cosh[(1 + j)y_0/\delta_\kappa]} \quad h_\nu = \frac{\cosh[(1 + j)y/\delta_\nu]}{\cosh[(1 + j)y_0/\delta_\nu]} \quad (7)$$

$$k_\kappa = \frac{\delta_\kappa}{1 + j} \frac{\sinh[(1 + j)y/\delta_\kappa]}{\cosh[(1 + j)y_0/\delta_\kappa]} \quad k_\nu = \frac{\delta_\nu}{1 + j} \frac{\sinh[(1 + j)y/\delta_\nu]}{\cosh[(1 + j)y_0/\delta_\nu]} \quad (8)$$

$$f_\kappa = \frac{\tanh[(1 + j)y_0/\delta_\kappa]}{[(1 + j)y_0/\delta_\kappa]} \quad f_\nu = \frac{\tanh[(1 + j)y_0/\delta_\nu]}{[(1 + j)y_0/\delta_\nu]} \quad (9)$$

and where Pr is the Prandtl number,  $\beta$  the thermal expansion coefficient,  $\gamma$  the ratio of isobaric to isochoric specific heat,  $\rho_0$  the mean density,  $T_0$  the time-averaged temperature,  $\delta_\nu = \sqrt{2\eta/\rho_0\omega}$  the viscous penetration depth ( $\eta$  being the shear viscosity coefficient) and  $\delta_\kappa = \sqrt{2K/\rho_0 c_p \omega}$  the thermal penetration depth ( $K$  being the gas thermal conductivity coefficient).

The longitudinal pressure gradient  $dp_1/dx$  along the HX assembly is calculated by imposing continuity of volume flow rate at the entrance of the HXs

$$\frac{dp_1}{dx} = \frac{\rho_0 \omega}{(1 - f_v)\Omega} v_0 \quad (10)$$

where the blockage ratio  $\Omega = A_{HX}/A_{res} = 1/(1 + l/y_0)$  describes the porosity of the HXs ( $A_{res}$  being the cross sectional area of the resonator and  $A_{HX}$  is the cross sectional area of the HXs open to gas flow). The gas temperature is governed by the general equation of energy conservation [13]:

$$\frac{\partial}{\partial t} \left( \frac{1}{2} \rho v^2 + \rho u \right) = -\nabla \cdot \dot{\mathbf{e}} \quad (11)$$

where  $u$  is the specific internal energy and where  $\dot{\mathbf{e}}$ , the energy flux density, is defined as

$$\dot{\mathbf{e}} = \rho \mathbf{v} \left( \frac{1}{2} v^2 + h \right) - \mathbf{v} \cdot \boldsymbol{\sigma} - K \nabla T \quad (12)$$

where  $h$  is the specific enthalpy and  $\boldsymbol{\sigma}$  the viscous stress tensor. Time averaging Eq. (10) over an acoustic cycle leads to

$$\nabla \cdot \bar{\dot{\mathbf{e}}} = 0 \quad (13)$$

where over-bar means time-averaged. Equation (13) is applied to each cell of the computational domain to impose the local energy balance. To accomplish this, a finite difference technique is employed where the quantitative results of standard linear theory are substituted for the  $x$  and  $y$  the components of the time-averaged energy flux density [13].

$$\bar{\dot{e}}_x = \frac{\omega}{2\pi} \left( \int_0^{2\pi/\omega} \rho v_x \left( \frac{1}{2} v^2 + h \right) dt - \int_0^{2\pi/\omega} (v_x \sigma_{xx} + v_y \tau_{xy}) dt - K \int_0^{2\pi/\omega} \frac{\partial T}{\partial x} dt \right) \quad (14)$$

$$\bar{\dot{e}}_y = \frac{\omega}{2\pi} \left( \int_0^{2\pi/\omega} \rho v_y \left( \frac{1}{2} v^2 + h \right) dt - \int_0^{2\pi/\omega} (v_x \tau_{xy} + v_y \sigma_{yy}) dt - K \int_0^{2\pi/\omega} \frac{\partial T}{\partial y} dt \right) \quad (15)$$

where

$$\sigma_{xx} = \frac{2}{3} \eta \left( 2 \frac{\partial v_x}{\partial x} - \frac{\partial v_y}{\partial y} \right) \approx -\frac{2}{3} \eta \frac{\partial v_y}{\partial y} \quad (16)$$

$$\tau_{xy} = \tau_{yx} = \eta \left( \frac{\partial v_x}{\partial y} + \frac{\partial v_y}{\partial x} \right) \approx \eta \frac{\partial v_x}{\partial y} \quad (17)$$

$$\sigma_{yy} = \frac{2}{3} \eta \left( 2 \frac{\partial v_y}{\partial y} - \frac{\partial v_x}{\partial x} \right) \approx \frac{4}{3} \eta \frac{\partial v_y}{\partial y} \quad (18)$$

the  $x$  velocity gradients having been neglected because of the order of  $\delta/\lambda$  being smaller than the  $y$  velocity gradients.

Making use of the complex notation and retaining only terms up to second order Eqs. (14) and (15) can be written as:

$$\bar{q}_x = \frac{1}{2} \rho_0 c_p \operatorname{Re} \{ T_1 \tilde{v}_{x1} \} + \frac{1}{3} \eta \operatorname{Re} \left\{ \frac{\partial v_{y1}}{\partial y} \tilde{v}_{x1} \right\} - \frac{1}{2} \eta \operatorname{Re} \left\{ \frac{\partial \tilde{v}_{x1}}{\partial y} v_{y1} \right\} - K \frac{\partial T_0}{\partial x} \quad (19)$$

$$\bar{q}_y = \frac{1}{2} \rho_0 c_p \operatorname{Re} \{ T_1 \tilde{v}_{y1} \} - \frac{1}{2} \eta \operatorname{Re} \left\{ \frac{\partial v_{x1}}{\partial y} \tilde{v}_{x1} \right\} - \frac{2}{3} \eta \operatorname{Re} \left\{ \frac{\partial v_{y1}}{\partial y} \tilde{v}_{y1} \right\} - K \frac{\partial T_0}{\partial y} \quad (20)$$

where energy flux densities have been converted to heat flux densities ( $\bar{e}_x \equiv \bar{q}_x, \bar{e}_y \equiv \bar{q}_y$ ) because in the short stack approximation the work flux contribution to the total energy flux is small [1]. The explicit expressions of these equations are reported in [12].

The calculation of the steady-state two-dimensional time-averaged temperature distribution is performed using a finite difference methodology where temperature spatial gradients are discretized using first order nodal temperature differences. To this end, the computational domain is subdivided using a rectangular grid. In the  $x$  direction the computation mesh size is typically  $0.005 L$  while in the  $y$  direction the computation mesh size is typically  $0.02 y_0$ . The imposed boundary conditions took into account: the symmetry on the nodal line at  $y=0$ ; the continuity of temperature and transverse heat fluxes at the gas-solid interfaces ( $y=y_0$ ); and the vanishing energy flux at the HX pore ends ( $x=0; x=2L$ ) facing the duct (gas oscillations outside the HXs are adiabatic and thus the thermoacoustic effect vanishes).

Applying Eq. (13) in each cell of the computational grid, a system of quadratic algebraic equations with respect of the unknown variable  $T_0$  is generated. The system is solved by a code developed by the authors in FORTRAN-90 language which executes the recursive Newton-Raphson method [14]. At each iteration the system of linear algebraic equations providing the temperature corrections for the next step is solved using a LU decomposition with partial pivoting and row interchanges matrix factorization routine. The latter is taken from the LAPACK library routines available online at [15], where details of the accuracy, computational cost, etc. can be found. Once the time-averaged temperature distribution is known, it can be substituted in Eqs. (19) and (20) to determine the energy flux distributions along the  $x$  and  $y$  directions in the gas. In the next section the code is validated by comparing numerical predictions against experimental measurements.

#### 4. Results and discussion

The temperature field measurements were performed in 20 phases within an acoustic cycle. Here, the most characteristic temperature distributions at six phases are presented to discuss the heat transfer process in an acoustic cycle. Figure 5 illustrates the temperature distribution in these six phases,  $\Phi_1(0^\circ)$ ,  $\Phi_6(90^\circ)$ ,  $\Phi_8(126^\circ)$ ,  $\Phi_{12}(198^\circ)$ ,  $\Phi_{16}(270^\circ)$  and  $\Phi_{18}(306^\circ)$ , for a Reynolds number equal to 250 (with the corresponding fluid displacement amplitude of 16 mm).

At phase  $\Phi_1$ , the fluid displacement reaches the maximum negative value, which indicates that the gas parcel moves the farthest to the left. The cold gas in the channel of the cold fin (referred as the cold channel thereafter) moves far into the channel of the hot fin (referred as the hot channel thereafter) and is heated by the plates. Some part of hot gas in the hot channel flows out of it and enters the open area behind the hot fins. It can be clearly seen that the gas in the top region behind the hot fins is heated up, due to the cumulative effect of natural convection over time. After this phase, the gas parcel starts to accelerate to move to the right. At phase  $\Phi_6$ , the cold gas heated by the hot fins partly flows out of the hot channel and enters into the cold channel. Hot gas entering from the open area behind the hot fins is dominant at the left end of hot channel. The gas parcel continues to move to the right. At phase  $\Phi_8$ , the hot gas has dominated the whole hot channel and partly penetrates into the cold channel. The cold gas in the cold channel partly moves into the open area behind the cold fins and mixes with the colder gas in this region. It can be found that the natural convection effect also exists. At phase  $\Phi_{12}$ , the gas parcel just starts to move to the left. The cold gas in the cold channel gradually moves into the hot channel and, at the same time, the cold gas in the open area behind the cold fins partly flows into the cold channel. At phase  $\Phi_{16}$ , the cold gas penetrates far into the hot channel and the hot gas in the hot channel also migrates

into the open area behind the hot fins. At phase  $\Phi_{18}$  the hot channel is occupied by the cold gas and the hot gas in the hot channel moves further to the left. After this phase, the gas parcel keeps moving to the left. Then another acoustic cycle repeats itself. Analogous processes can be identified at the higher Reynolds number where the relatively large velocity develops a very thin thermal boundary layer.

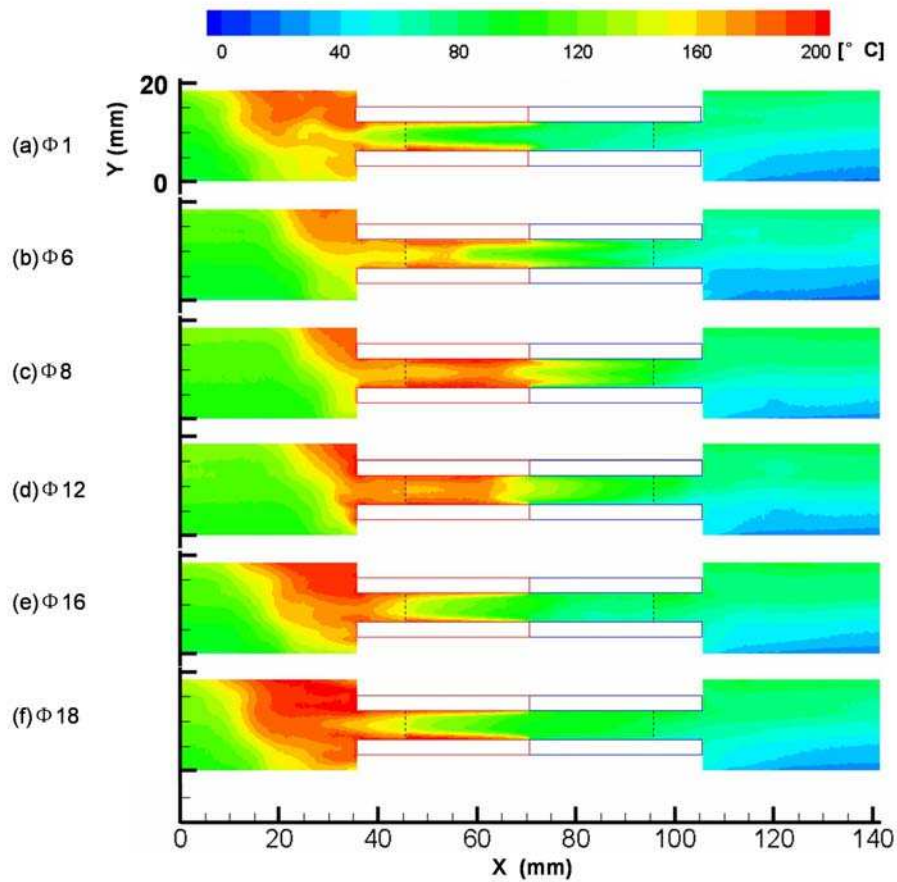


**Figure 5.** Temperature distributions for six selected phases and for  $Re=250$ . Red rectangles mark the heated plates and blue rectangles mark the cooled plates in the heat exchanger assembly. The black dashed lines mark the position where the three views (left, central and right) join to one another

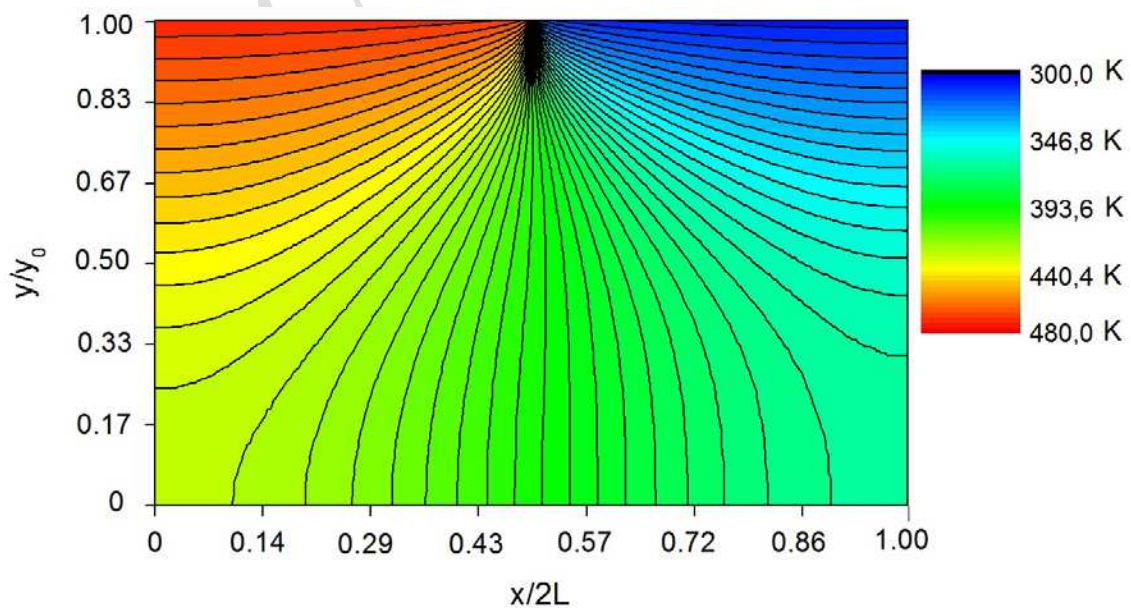


**Figure 6.** Time averaged temperature distribution in half a gas channel generated by the computational model for  $Re=250$ .

For comparison, in Fig. 6 the time-averaged temperature distribution generated by the computational model is shown for the same value of the Reynolds number. At the joint position and in the mid channel regions (far from the fin surface) the temperature is nearly uniform over a cross section (isotherms are vertical). In the direction away from the joint towards both the cold and hot channel the isotherms become even more curved and practically horizontal at the gas-solid interface. Isotherms, however, become more densely packed when approaching the joint point and this trend is compatible with a growing transverse temperature gradient  $\partial T_0/\partial y$  near this region. The joint involves a great temperature gradient in both the longitudinal and the transverse direction and most of the heat transfer between the gas and the plate should be localized in this region. This is confirmed by the longitudinal distribution of the transverse heat flux density at the gas-solid interface calculated by Eq. 19. Results are shown in Fig.7 at selected Reynolds numbers.

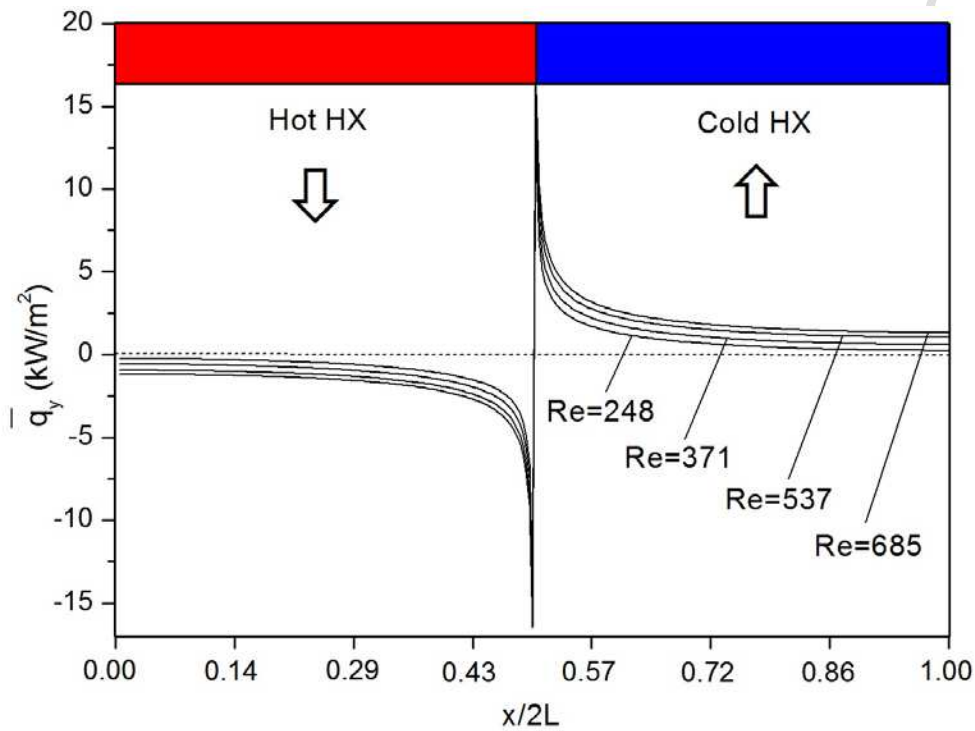


**Figure 7.** The time-averaged transverse heat flux density at the hot and cold fin surface ( $y=y_0$ ) as a function of the axial coordinate for selected Reynolds numbers.

Since the time-averaged transverse energy flux at the plate surface is positive when entering the plate and negative when leaving the plate, Fig. 7 implies that over the period of an acoustic cycle, energy flows out of the hot fin on the left, then hydrodynamically along the thermal boundary layer in the gas and into the cold fin on the right.

Information on the time evolution of the heat flux exchanged between the oscillating gas and the solid fins can be obtained from the cross sectional temperature profiles. In Fig. 8 the transverse temperature profiles measured 1mm away from the centre of the HX assembly both in the cold and hot fin are illustrated for the previously selected six phases and for  $Re=250$ . The six phases denoted with red symbols correspond to the position in the hot channel 1 mm away from the “joint”, while the other six phases denoted with blue symbols correspond to the position in the cold channel 1 mm away from the “joint”. The distance from the fin surface is normalized by the channel width,  $2y_0 = 6$  mm while the gas temperatures are normalized by

$$\theta = \frac{T - T_w}{T_H - T_C} \quad (21)$$

$T$ ,  $T_w$ ,  $T_H$  and  $T_C$  being the instantaneous gas temperature, wall (fin) temperature, reference hot temperature (200°C) and reference cold temperature (30°C), respectively. The temperature profiles clearly show the large temperature variations in a very thin layer of gas near the wall. For all six phases in the hot channel the heat transfer direction is from the plate to the gas, while in the cold channel the heat is always transferred from the gas to the plate. It is also found that in the cold channel at phase  $\Phi_1$ , the temperature of the gas beyond the thin layer near the wall is lower than the wall temperature (a negative  $\theta$ ). It is understood that at this phase the gas parcel is in the left-most position and the cold gas from the cold channel moves deeply into the hot channel. The colder gas from the right takes over this position. This part of gas affects the processes for a while so that at phase  $\Phi_6$  the temperature in the centre of the cold channel is still lower than the wall temperature.

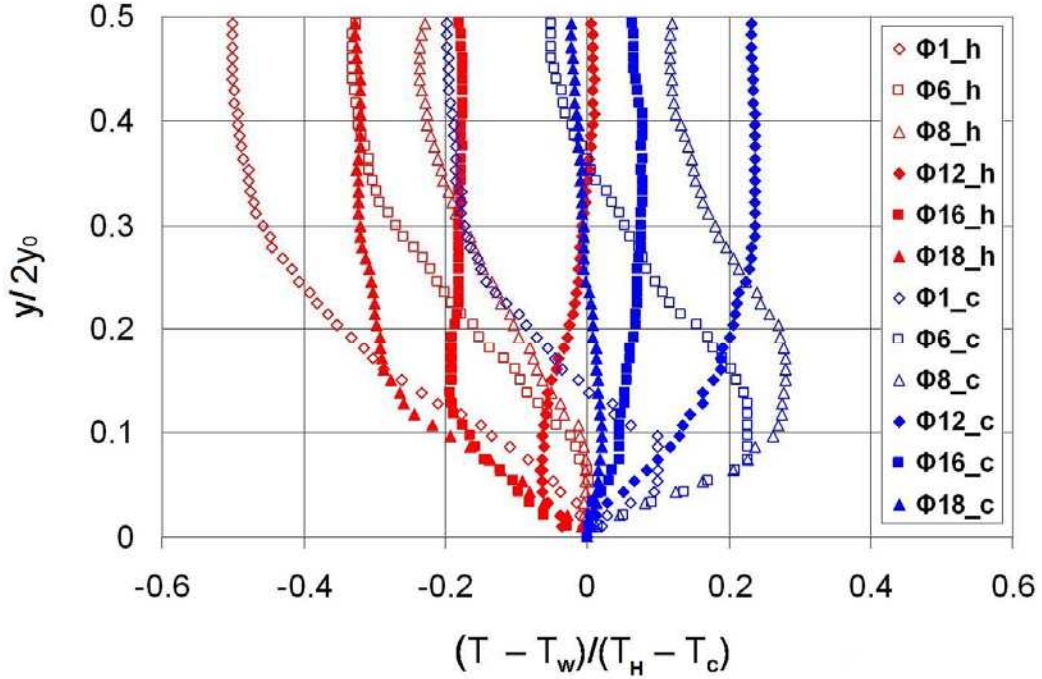


**Figure 8.** Cross sectional temperature profiles measured 1mm away from center of the HX assembly both in the cold and in the hot fin for the previous selected six phases and for  $Re=250$ .

The temperature profiles enable calculation of local, phase-dependent, transverse heat flux densities on the HX surface from first principles:

$$q_y(x, \Phi) = -K \left. \frac{dT(x, y, \Phi)}{dy} \right|_{y=y_0} \quad (22)$$

Integrating Eq. (22) in phase over an acoustic cycle and/or in space over the fin length it is possible to obtain time-averaged and/or space averaged heat flux densities. In particular, phase-and-area averaged heat transfer coefficients are calculated as

$$h = \frac{1}{2\pi L} \int_0^L dx \int_0^{2\pi} [q_y(x, \Phi)/(T_w - T)] d\Phi. \quad (23)$$

$T$  is the reference fluid temperature evaluated in the centre of the channel, at the same stream-wise location as the joint between hot and cold channels. The values of  $h$  can then be converted into non-dimensional Nusselt numbers based on the fin thickness  $2l$ :

$$Nu = \frac{h(2l)}{K} \quad (24)$$

Note that when manipulating data generated by the computational model the phase integration is not required since the model directly provides time averaged quantities.

The comparison between the experimental and computational data is presented in Fig. 9 in terms of the area-and-phase averaged transverse heat flux density at the fin surface. The graph clearly shows that the two fins exhibit a rather different behaviour. The heat flux exchanged at the hot HX (open circles) appears to be an increasing function of the Reynolds number. This is due to the high velocity and displacement amplitudes at high Reynolds numbers which increase the temperature gradient in the hot and cold channel. The heat flux exchanged by the cold HX (full circles) reaches a maximum for  $Re=535$ . This behaviour can be interpreted as an effect of the variation of the effective length of heat transfer with the gas displacement amplitude. At low Reynolds number, in fact, the gas displacement amplitude is less than the length of hot and cold HX, so the gas portion heated by the hot exchanger can only partly transfer heat to the cold HX. In particular, the gas heated at the left-most end of the hot HX cannot exchange heat with the cold HX.

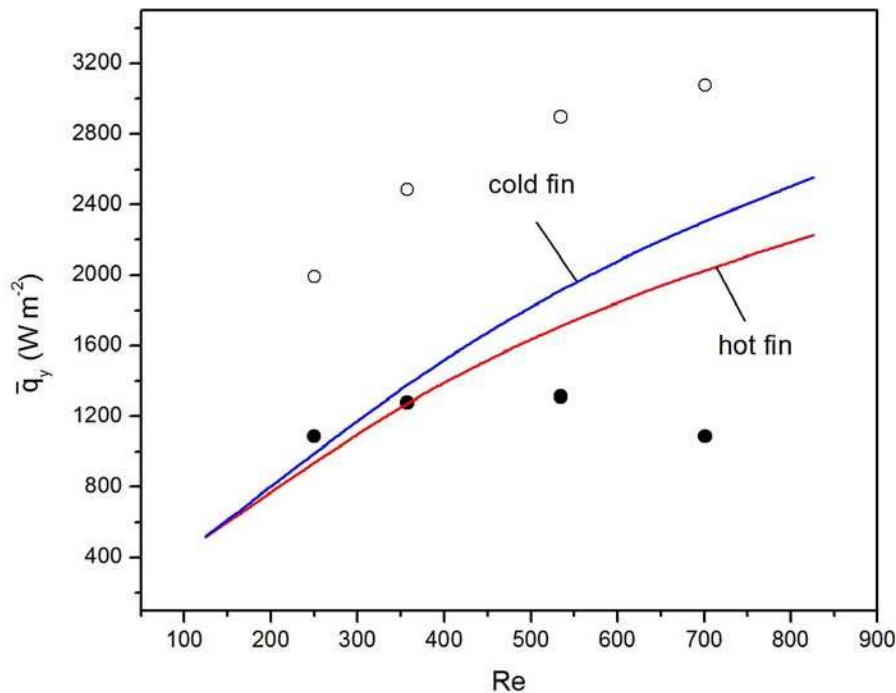


**Figure 9.** Area-and-phase averaged transverse heat flux at the cold (full circles) and hot (open circles) heat exchanger. Solid lines are predictions of the simulation model

When the Reynolds number is 535, the corresponding gas displacement amplitude is 36 mm, which is close to the length of hot and cold HX (35 mm). In this case the gas heated by the hot HX can fully transfer heat to the cold HX. When the gas displacement exceeds the length of hot and cold heat HXs, the colder gas from outside of the hot HX moves into the cold HX and cannot effectively exchange heat with the cold HX. In the considered Re range the experimental heat fluxes are matched by the computational ones with an error of about 40%. The model is able to take into account the “saturation” of the heat transfer at increasing Re numbers (the growth of the curves diminishes with Re) but not the maximum observed in  $\bar{q}_y$  at the cold HX. Furthermore, in contrast with experiment, the heat exchanged by the cold HX appears to be higher than the heat exchanged by the hot HX. This result is not surprising since in the proposed model the channel ends are considered as thermally insulated, based on the hypothesis that oscillations in fluid outside the HXs are adiabatic, and so no energy can escape from the channel. Thus, the cold HX is loaded by the heat delivered by the hot HX plus eventually the heat generated by viscous dissipation at the solid walls.

However, Fig. 5 clearly shows that a large fraction of the heat transmitted to the gas by the hot HX is spread out in the resonator hot duct by free convection. This phenomenon is not negligible at the hot duct side since its strength is proportional to  $d^3$ , ( $d=134$  mm being the side of the resonator's square cross section) and to the difference between the mean temperature of the gas leaving the hot HX pores and the mean temperature of the hot duct (approximately the difference between 150 and 200°C). At the cold duct side the free convection process is much less marked due to the lower temperature difference between the gas and cold duct (nearly zero). Inside the HX channels the phenomenon is clearly negligible since  $2y_0 \ll d$ , as confirmed by inspection of Fig 5 that reveals that the gas-fin heat exchange is symmetric along the transverse  $y$  direction. This provides an “*a posteriori*” justification of the reduced computational domain selected on the basis of the (assumed) symmetry of the problem along the  $y$  coordinate.

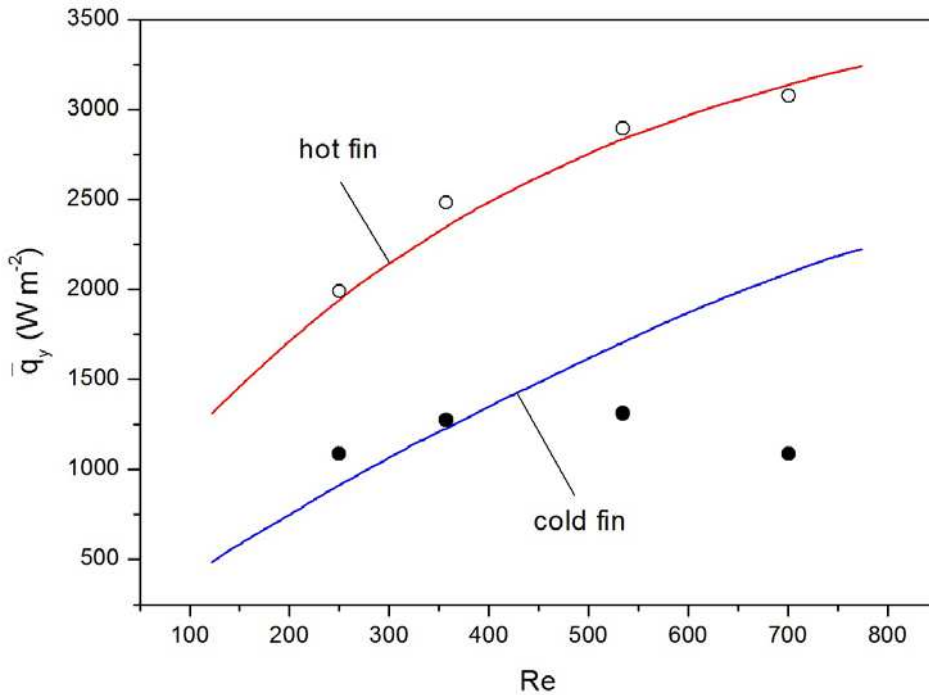


**Figure 10.** Area-and-phase averaged transverse heat flux at the cold (full circles) and hot (open circles) HX. Solid lines are predictions of the simulation model modified to account for heat leakage to the resonator duct

The strong free convection processes taking place at the hot duct side facing the HXs assembly entail, however, that the hypothesis of considering the gas oscillations just outside the hot HX fins as adiabatic (applied in the implementation of the model) is probably no longer valid. These circumstances are responsible for the higher measured heat transfer rates at the hot HX compared to those computed by the model, and for the breakdown of the  $y$  symmetry at the inlet and outlet of the HX pores.

Therefore, as a first step to take into account these very complex free convection processes in the framework of the simplified computational model used, the numerical code has been modified by introducing two fictitious thermal reservoirs on both the side of the cold duct and the side of the hot duct. These thermal reservoirs are modelled to thermally interact with the oscillating gas inside the HX channel through two heat transfer coefficients that, in addition to the thermal reservoir temperatures, are considered as fitting parameters. Results are shown in Figs. 10 and 11 in terms of the transverse heat fluxes and the Nusselt numbers. The corresponding heat leakages to the hot and cold side of the duct computed by the simulation model are reported in Fig. 12.

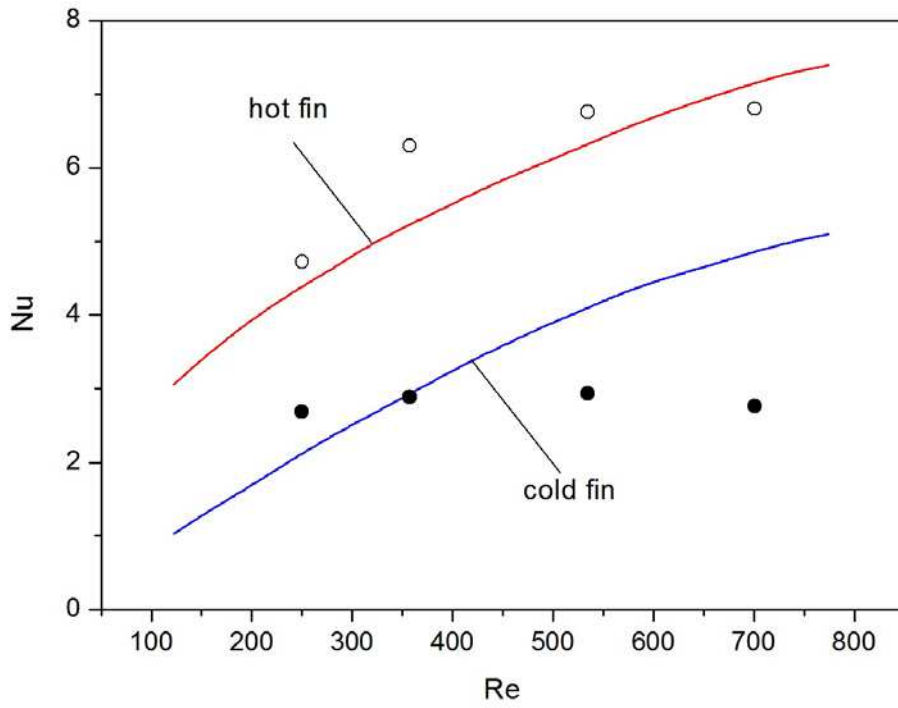


**Figure 11.** Area-and-phase averaged Nusselt numbers at the cold (full circles) and hot (open circles) heat exchanger. Solid lines are predictions of the simulation model modified to account for heat leakage to the resonator duct.

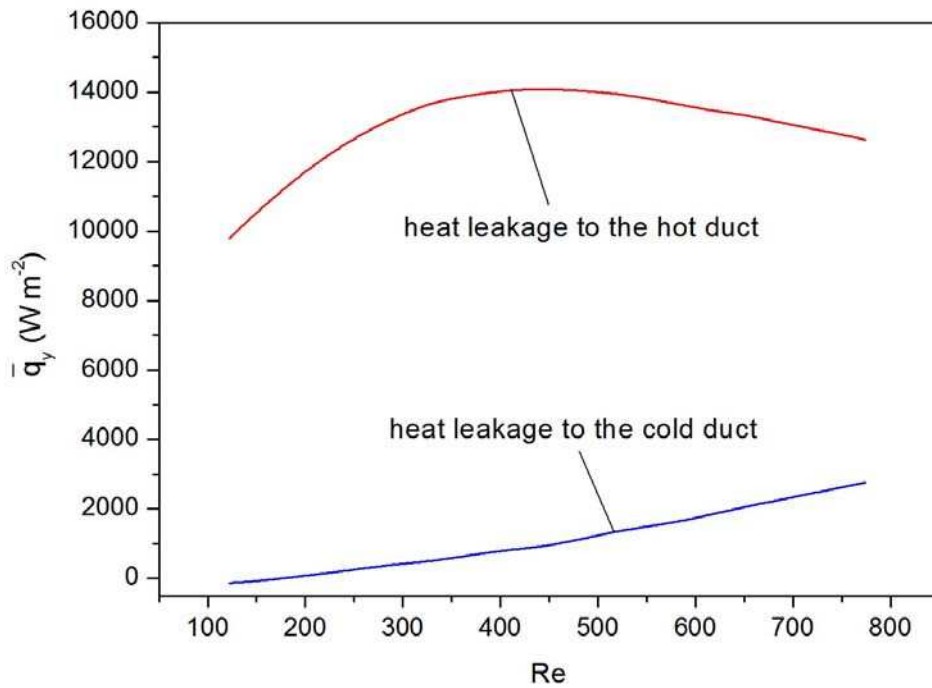


**Figure 12.** Numerically computed heat leakages to the hot side and cold side of the resonator duct

The experimental data are now described by the simulation curves with an error of 3% and 35% at the hot and cold HX, respectively. The measured Nusselt numbers exhibit a dependence on Re similar to that of  $\bar{q}_y$  (Fig. 11). A maximum in Nu evaluated at the cold HX for Re=535 is observed to which a saturation in Nu evaluated at the hot HX corresponds. The experimental Nu numbers are fitted by the numerical model with an error of 9% and 35% at the hot and cold HX, respectively.

The previous analysis suggests that in the investigated range of flow conditions,  $Re=535$  is the optimal flow parameter for the thermal performance of the tested HXs. This is likely due to the circumstance that the gas displacement amplitude equals the length of the hot and cold exchanger for this Reynolds number. Heat transfer coefficients from the gas-side can be predicted with a confidence of about 40% at moderate acoustic Reynolds numbers. The matching of the experimental data improves if heat transport from the couple of HXs to the surrounding environment (hot and cold ducts) is considered. These heat losses are most likely caused by the entrance/exit effects localized at the resonator-HX cross section interfaces which are responsible of complex non-linear temperature and flow patterns (strong vortex flows and turbulence generation effects [16,17]). Although the simplified model proposed to account for this effect doesn't constitute at this stage a predictive algorithm for quantitative estimations, it provides some evidence that this kind of phenomena could have a non-negligible influence on the value of the heat transfer coefficients at the gas side of the HXs (especially at the hot HX). Further experimental investigations and theoretical modelling are required for more detailed insight into the physics of thermo-fluid processes.

## 5. Conclusions

The work described in this paper utilises the novel measurement techniques developed in order to obtain instantaneous temperature and velocity fields in the interstices of the internal structures of thermoacoustic devices. This is a challenging task, which has not been attempted before, and which enables a unique insight into the physics of thermofluids processes within the oscillatory compressible flows that govern the associated energy transfer. Acetone-based Planar Laser Induced Fluorescence (PLIF) and Particle Image Velocimetry (PIV) techniques have been applied to obtain spatially and temporally resolved temperature and velocity fields within parallel-plate thermoacoustic heat exchangers. The local temperature distribution profiles within an acoustic cycle and space-averaged phase-dependent heat fluxes reveal the heat transfer variations phase by phase. The dependence of the space-cycle averaged heat fluxes and the Nusselt numbers on the Reynolds number shows that the optimal performance of heat exchangers can be achieved when the gas displacement amplitude is close to the length of hot and cold heat exchanger.

The experimental data obtained from the measurement of the temperature field provide an important reference for validation of a CFD code implemented on the basis of the classical thermoacoustic linear theory. Comparisons between the detailed spatially- and temporally-resolved measurements provide a unique opportunity to test the predictive capabilities of the CFD code developed in the course of this research. It is shown that the code is able to predict heat transfer coefficients from the gas-side with a confidence of about 41% at moderate acoustic Reynolds numbers. However, better estimates can be achieved when the entrance/exit effects localized at the resonator-HX cross section interfaces are taken into account. These effects are responsible for considerable heat losses from the couple of heat exchangers into the surrounding environment (the resonator extending beyond the heat exchangers). The results of this study demonstrate the need for developing the new thinking for the design of CFD codes to encapsulate the nature of thermal-fluid interactions present in the thermoacoustic devices, and in the long term to encourage new paradigms and concepts for the future design of heat exchangers in thermoacoustic systems.

## Acknowledgments

This research is financially supported by the European Commission under the FP7 framework grant THATEA: THERMOACOUSTIC TECHNOLOGY FOR ENERGY APPLICATIONS (Grant 226415 – FP7-ENERGY-2008-FET). Dr Xiaohan Mao of Leicester University is acknowledged for collecting the PLIF data used in this paper.

## References

- [1] G.W. Swift, Thermoacoustic engines, *Journal of the Acoustical Society of America* 84 (1988) 1145-1180
- [2] G.W. Swift, *Thermoacoustics: A unifying perspective for some engines and refrigerators*, Acoustical Society of America, 2002
- [3] S. Backhaus, G.W. Swift, A thermoacoustic Stirling heat engine: detailed study, *Journal of the Acoustical Society of America* 107 (2000) 3148-3166
- [4] G.W. Swift, Analysis and performance of a large thermoacoustic engine, *Journal of the Acoustical Society of America* 92 (1992) 1551-1563
- [5] S.L. Garret, D.K. Perkins, A. Gopinath, Thermoacoustic refrigerator heat exchangers: design, analysis and fabrication, in: G.F. Hewitt (Ed.), *Proceedings of the Tenth International Heat Transfer Conference*, Brighton, UK, 1994, pp 375-380
- [6] A. Piccolo, G. Pistone, Estimation of heat transfer coefficients in oscillating flows: the thermoacoustic case, *International Journal of Heat and Mass Transfer* 49 (9-10) 2006, 1631-1642
- [7] I. Paek, J.E. Braun, L. Mongeau, Characterizing heat transfer coefficients for heat exchangers in standing wave thermoacoustic coolers. *Journal of the Acoustical Society of America*, 118 (4) (2005) 2271-2280
- [8] A. Berson, M. Michard, P. Blanc-Benon, Measurement of acoustic velocity in the stack of a thermoacoustic refrigerator using particle image velocimetry, *Heat and Mass Transfer* 44 (8) (2008) 1015-1023
- [9] G. Mozurkewich, Heat transfer from transverse tubes adjacent to a thermoacoustic stack, *Journal of the Acoustical Society of America* 110 (2) (2001) 841-847
- [10] E.C. Nsofor, S. Celik, X. Wang, Experimental study on the heat transfer at the heat exchanger of the thermoacoustic refrigerating system, *Applied Thermal Engineering* 27 (2007) 2435-2442
- [11] L. Shi, X. Mao and A. J. Jaworski, Application of planar laser-induced fluorescence measurement techniques to study the heat transfer characteristics of parallel-plate heat exchangers in thermoacoustic devices, *Measurement Science and Technology* 21 (2010) 115405 (16p).
- [12] A. Piccolo, Numerical computation for parallel plate thermoacoustic heat exchangers in standing wave oscillatory flow. *International Journal of Heat and Mass Transfer* 54 (21-22) (2011) 4518-4530
- [13] L.D. Landau, E.M. Lifshitz, *Fluid Mechanics*, first ed., Pergamon, London, 1959
- [14] W.H. Press, S.A. Teukolsky, W.T. Vetterling, B.P. Flannery, *Numerical recipes in Fortran*, Snd. Ed., 1994, Cambridge University Press
- [15] <http://www.netlib.org/lapack>
- [16] L. Shi, Z.B. Yu, A.J. Jaworski, Vortex shedding flow patterns and their transitions in oscillatory flows past parallel-plate thermoacoustic stacks. *Experimental Thermal and Fluid Science* 34 (7) (2010) 954-965
- [17] X. Mao, A.J. Jaworski, Application of particle image velocimetry measurement techniques to study turbulence characteristics of oscillatory flows around parallel-plate structures in thermoacoustic devices. *Measurement Science and Technology*, 21 (3) (2010), 035403 (16pp)